Astronomy & Astrophysics

Deep learning inference with the Event Horizon Telescope

III. ZINGULARITY results from the 2017 observations and predictions for future array expansions

M. Janssen[1,2,*] , C.-k. Chan[3,4,5], J. Davelaar[6,**], and M. Wielgus[7]

[1] Department of Astrophysics, Institute for Mathematics, Astrophysics and Particle Physics (IMAPP), Radboud University, PO Box 9010, 6500 GL Nijmegen, The Netherlands
[2] Max-Planck-Institut für Radioastronomie, Auf dem Hügel 69, 53121 Bonn, Germany
[3] Steward Observatory and Department of Astronomy, University of Arizona, 933 N. Cherry Ave., Tucson, AZ 85721, USA
[4] Data Science Institute, University of Arizona, 1230 N. Cherry Ave., Tucson, AZ 85721, USA
[5] Program in Applied Mathematics, University of Arizona, 617 N. Santa Rita Ave., Tucson, AZ 85721, USA
[6] Department of Astrophysical Sciences, Peyton Hall, Princeton University, Princeton, NJ 08544, USA
[7] Instituto de Astrofísica de Andalucía-CSIC, Glorieta de la Astronomía s/n, 18008 Granada, Spain

ABSTRACT

Context. In the first two papers of this publication series, we present a comprehensive library of synthetic Event Horizon Telescope (EHT) observations and used this library to train and validate Bayesian neural networks for the parameter inference of accreting supermassive black hole systems. The considered models are ray-traced general relativistic magnetohydrodynamic (GRMHD) simulations of Sgr A* and M87*.
Aims. In this work, we infer the best-fitting accretion and black hole parameters from 2017 EHT data and predict improvements that will come with future upgrades of the array.
Methods. Compared to previous EHT analyses, we considered a substantially larger synthetic data library and the most complete set of information from the observational data. We made use of the Bayesian nature of the trained neural networks and apply bootstrapping of known systematics in the observational data to obtain parameter posteriors.
Results. Within a wide GRMHD parameter space, we find M87* to be best described by a spin between 0.5 and 0.94 with a retrograde MAD accretion flow and strong synchrotron emission from the jet. Sgr A* has a high spin of ~0.8–0.9 and a prograde accretion flow beyond the standard MAD/SANE models with a comparatively weak jet emission, seen at a $\sim 20°$–$40°$ inclination and $\sim 106°$–$137°$ position angle. While previous EHT analyses could rule out specific regions in the model parameter space considered here, we are able to obtain narrow parameter posteriors with our ZINGULARITY framework without being impacted by the unknown foreground Faraday screens and data calibration biases. We further demonstrate that the Africa Millimeter Telescope extension to the EHT will reduce parameter inference errors by a factor of three for non-Kerr models, enabling more robust tests of general relativity.
Conclusions. Our results agree with multiwavelength constraints from the literature. It will be instructive to produce new GRMHD models with the inferred interpolated parameters for in depth model-data comparisons and to study their accretion rate plus jet power.

Key words. accretion, accretion disks – black hole physics – techniques: high angular resolution – techniques: interferometric – galaxies: active

1. Introduction

With the Event Horizon Telescope (EHT), we imaged the supermassive black holes in the centers of Messier 87* (M87*, Event Horizon Telescope Collaboration 2019a) and Sagittarius A* (Sgr A*, Event Horizon Telescope Collaboration 2022a). In Event Horizon Telescope Collaboration (2019d, 2022d, 2021b, 2023, 2024), selections of general relativistic magnetohydrodynamics (GRMHD) models are scored against specific observational EHT and multiwavelength data products.

The scoring is facilitated through electromagnetic observables computed from the GRMHD models; the synchrotron emission at a wavelength of 1.3 millimeter is predicted with

general relativistic ray-tracing methods (e.g., Gold et al. 2020; Prather et al. 2023). Below, we list the key physical parameters of interest in the ray-traced GRMHD models considered in this study:

1. Given the black hole mass M and angular momentum J measured with respect to the accretion flow, the dimensionless black hole spin a_*, given via $a_* = cJG^{-1}M^{-2}$, where c and G are the speed of light and the gravitational constant, respectively. For our "standard" models that we mostly considered here, the static Kerr spacetime metric (Kerr 1963) varies only with a_*, as we fix the masses for Sgr A* and M87* to be $4.14 \times 10^6 \, M_\odot$ and $6.2 \times 10^9 \, M_\odot$, respectively.

2. For the considered Kerr-Newmann solutions, the dimensionless black hole charge q_* (Newman et al. 1965). These models were ray-traced only in Stokes $\mathcal{I}$.

---

* Corresponding author: M.Janssen@astro.ru.nl
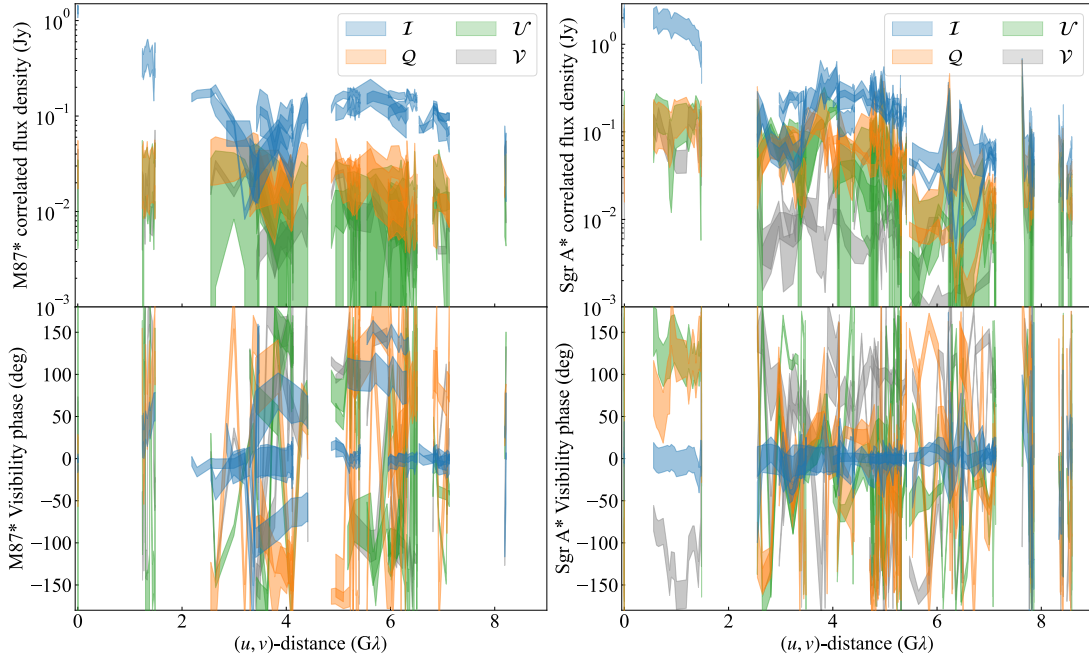** NASA Hubble Fellowship Program, Einstein Fellow

Fig. 1. Correlated flux densities in Jansky (Jy) and visibility phases in degrees (deg) with standard deviation error bands computed from 1000 bootstrapping realization of the 2017 April 11 M87* (left panels) and April 7 Sgr A* (right panels) observational EHT data. The measurements are plotted as a function of baseline length in units of the λ1.3 mm observing wavelength. The displayed Stokes parameters show the total intensity ($\mathcal{I}$), linear polarization ($\mathcal{Q}$&$\mathcal{U}$), and circular polarization ($\mathcal{V}$).

3. For the models that go beyond general relativity, the influence of a dilaton scalar field in the Einstein–Maxwell–Dilaton–Axion theory of gravity (García et al. 1995). The dilaton GRMHD models used in this work are described in detail in Mizuno et al. (2018) and Röder et al. (2023). These models were ray-traced only in Stokes $\mathcal{I}$.

4. The MAD or SANE magnetic state of the accretion disk (Event Horizon Telescope Collaboration 2019c, 2022d). Most MAD models are more variable and launch more powerful jets compared to their SANE counterparts.

5. The coupling between the temperatures of the protons and electrons R_{high} (Mościbrodzka et al. 2016). It is mostly the temperature of the electrons in the accretion disk and less so the strongly magnetized jet region that is sensitive to the R_{high} parameter.

6. For Sgr A*, the orientation (or position angle) θ_{PA} of the source on the sky and the inclination angle i_{los}, with which the source is oriented with respect to our line of sight. Both θ_{PA} and i_{los} parameters are measured relative to the accretion flow angular momentum vector.

In Janssen et al. (2025a), a library of synthetic EHT observations of M87* and Sgr A* are created from a library of GRMHD simulations that span the model parameter space listed above. Those parameters are then used as labels for the synthetic data to enable the supervised learning of Bayesian artificial neural networks (BANNs). We make use of the ZINGULARITY framework for the BANN training and validation, as described in Janssen et al. (2025b). Here, we applied two trained networks to observational Sgr A* and M87* EHT data.

Compared to previous EHT analyses, we utilized higher-quality observational data produced by an improved calibration scheme as described in Janssen et al. (2025a). Furthermore, we considered a wider range of GRMHD models and systematics that affect the EHT data than prior works. Our BANN implementations were trained to infer GRMHD model parameters based on salient features in the M87* and Sgr A* EHT data with conservative uncertainty estimates (Janssen et al. 2025b). For the GRMHD parameter inference, we considered the full Stokes information content of the EHT for the first time, instead of relying on derived data quantities.

In Section 2 of this work, we describe the data used for the BANN training and parameter inference. In Section 3, we briefly review the training of our networks and then show the results when applying the trained BANNs to observational data in Section 4. These results are discussed in Section 5 and we present our conclusions in Section 6. We finish with a description of the data and code availability, allowing others to reproduce our results.

2. Data

The EHT interferometric array measures Fourier components of the sky brightness distribution at millimeter wavelengths. The coverage of the projected baseline vectors between pairs of EHT antennas is commonly given as (u, v) vectors in units of the observing wavelength.

The observational data used in this work was taken by the EHT in 2017 (Event Horizon Telescope Collaboration 2019b, 2022b) within a 226.1–228.1 GHz frequency band. We based our analysis on the (u, v) coverage and data taken on April 7 for Sgr A* observations and April 11 for M87*. The coverage and noise properties of the measurements were used for the neural network training with GRMHD synthetic data (Janssen et al. 2025a). Amplitudes and phases of the observational data used for the subsequent GRMHD parameter inference are shown in Figure 1.

Synthetic datasets with parameters close to our BANN posteriors are shown in Figure 2, alongside their corresponding ground-truth GRMHD models. Here, we can see how only the
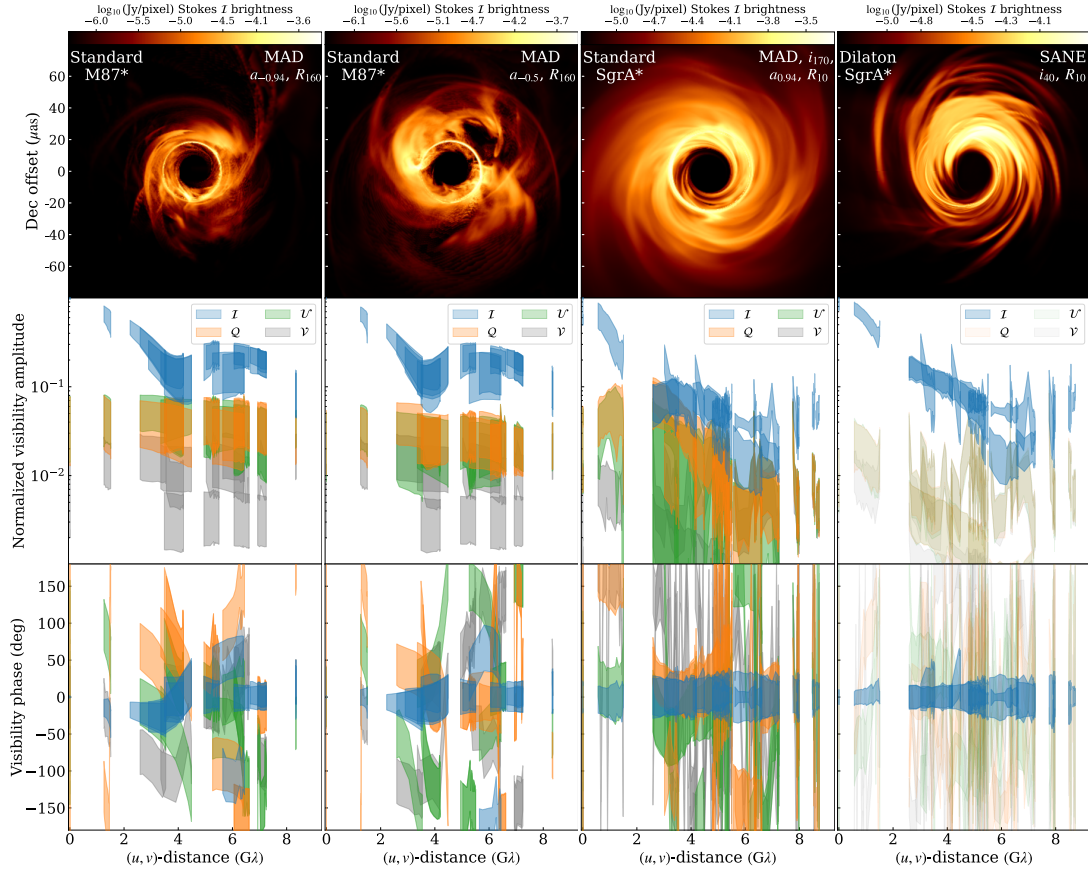
Fig. 2. Visualization of training datasets with parameters close to our best-fitting BANN inferences. The top row displays example total intensity ray-traced ground-truth model images on logarithmic scales with varying dynamic ranges. Top left corners show the type of model, top right corners show the model parameters: spin $a_* = s$, $R_{high} = r$, and $i_{los} = l$ parameters are listed in a shorthand notation as a_s, R_r, and i_l. The Sgr A* models are displayed here with $\theta_{PA} = 0$. The standard models are based on the Kerr metric (see Section 3 text). Distributions of normalized visibility amplitudes and phases with standard deviation error bands computed from all synthetic data training samples of each model are plotted in the middle and bottom rows, respectively. These visibilities are depicted for all Stokes parameters. For the unpolarized dilaton models, the polarized data probes only instrumental effects and are faded out.

linear polarization data shows distinguishing features between the two M87* models with different spins. We note that we generally do not expect an exact match between the Figure 1 observational and Figure 2 synthetic data. Firstly, the Figure 2 models only roughly match the inferred optimal parameters by our BANNs; a limitation of the GRMHD sampling. We know that small changes in model parameters can have significant effects on the visibility data (Section 7.3 of Janssen et al. 2025b). Secondly, the BANN inference does not use all of the data equally but focuses on salient features that can be used to differentiate between model parameters. For example, the Stokes $\mathcal{U}$ phase of Sgr A* at a (u, v)-distance of around $1 G\lambda$, which is sensitive to the larger scale orientation of the polarization, does not match between the shown Kerr ("standard") polarized Sgr A* model data and the observations. Given the similarity of the model parameters, the Stokes $\mathcal{I}$ visibilities from the Kerr and dilaton Sgr A* models are similar even though the underlying spacetime metrics are different.

We made use of observational 'CASA' data calibrated with the RPICARD (Janssen et al. 2018, 2019) pipeline. The characteristics of the BANN training sets are akin to the CASA data (Roelofs et al. 2020). In Janssen et al. (2025a), we presented a recent upgrade to the CASA data, which we make use of for the first time here, and describe the synthetic training data generation process in detail.

3. Neural network training

We used the ZINGULARITY framework to select the best BANN architectures for Sgr A* and M87* from a survey and trained them on our GRMHD synthetic data library as described in Janssen et al. (2025b). For Kerr Sgr A*, we two equally viable models, that only differ in the number of training epochs (60 vs. 50). For our other networks (M87* and dilaton Sgr A*), we found single sets of best parameters that are used to make single fiducial models. For the training, we used the Swish activation function (Ramachandran et al. 2017) and RMSProp optimization algorithm. For both Sgr A* and M87*, we employed similar network architectures, but with different numbers of connections and regularization methods. These hyperparameters were determined through parameter surveys. The employed Bayesian architecture is a combination of a ResNet (He et al. 2015) with subsequent variational fully connected layers.

The network training diagnostics of our fiducial models can be compared against our exotic models shown in the same Figure 3. Similarly, we can compare the capabilities of the current EHT to predictions for planned array upgrades. For our standard Sgr A* and M87* BANNs, we achieved typical validation errors of about 10% and 0.3%, respectively.

The synthetic data generation process and BANN architectures used for the training are the same for the standard and
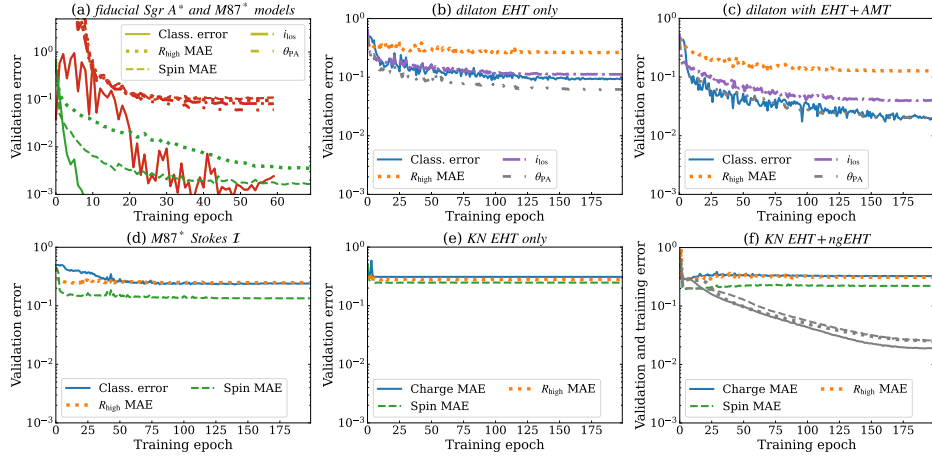
Fig. 3. ZINGULARITY performance diagnostics for various neural network training runs. The validation error is computed from normalized labels of validation data not seen by the network during training. The mean absolute error (MAE) is computed as the average of all validation samples for normalized regression labels. The classification error (Class. error) is defined as one minus the network's accuracy, i.e., the fraction of misclassified validation samples. Panel a shows the fiducial models for Sgr A* and M87* in red and green, respectively. Here, we show the Sgr A* model with a training length of 60 epochs; the 50 epoch model looks equivalent. For M87*, validation errors are overall smaller compared to Sgr A* and the classification errors get numerically close to zero beyond the logarithmic y-axis limit displayed in the figure here. Panel f also shows the training errors as gray curves.

exotic models. As the exotic models were ray-traced only in total intensity, the training is limited to Stokes $\mathcal{I}$ data, leading to relatively poor performance. For the dilaton models, we see a similar network performance compared to the Sgr A* Stokes $\mathcal{I}$ test of Janssen et al. (2025b). A comparison of panel b with c shows how the planned Africa Millimeter Telescope (AMT, Backes et al. 2016) improves validation errors of the dilaton model parameters by a factor of three on average. For a fair comparison, we used the same 2017 EHT antennas with identical sensitivities in both cases. We attribute the strong impact of the AMT primarily to the increased northeast and southwest resolution (La Bella et al. 2023) as well as the close (u, v) baselines from the South Pole to Chile and the AMT. These "crossing" tracks can be used to remove systematics from the data after the close-together Chile sites have been calibrated based on the total flux density of the source (e.g., Section 4.2 in Janssen et al. 2022).

The bottom panels of Figure 3 present our network training tests for Kerr-Newman models. As a baseline test, we first train on our standard Sgr A* models when only using total intensity data: Validation errors close to 10% are reached only for the spin parameter, as shown in panel d. For the Kerr-Newman models, the network failed to train on the synthetic data and no reliable estimations could be obtained for any parameter, as shown in panel e. We attribute the failure of fitting spin to the degeneracy with charge in the Kerr-Newman metric (Janssen et al. 2025a). With additional dishes from the ngEHT project (Doeleman et al. 2019, 2023) joining EHT observations, only marginal improvements can be achieved, as shown in panel (f). The errors on the training data itself follow the validation errors in a to e. For f, the training error differs from the validation error and is decreasing. With the amount of data from the extended baseline coverage, it will likely be possible to find a suitable network architecture to train on the Kerr-Newman features without the problematic overfitting seen here.

4. GRMHD parameter inference

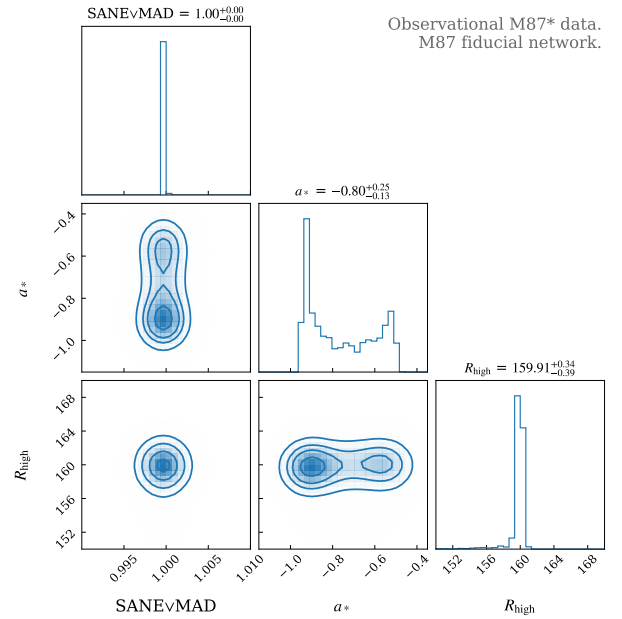For each observational dataset, we created 1000 bootstrapped realizations with varying polarization leakage, partially

Fig. 4. Posterior obtained from 10^6 variational inference draws of 1000 bootstrapped realizations of the observational M87* data with our fiducial M87* BANN. For the magnetic state, a value of zero corresponds to a certain SANE classification, and a value of one to a certain MAD classification.

correlated telescope gain plus gain curve errors, and thermal noise as described in Section 6.2 of Janssen et al. (2025b). Parameter posteriors were formed from 1000 inference passes through our BANNs for each realization of the observational data.

Figure 4 shows the results from applying our fiducial M87* BANN to the April 11 observational data. The data favor MAD models with a large $R_{high} = 160$ parameter. These models produce powerful outflows with a strong jet contribution to the synchrotron emission. The training data had a maximum R_{high} value of 160, so it might be that a model with an even higher R_{high} would describe the data better. The equivalent high
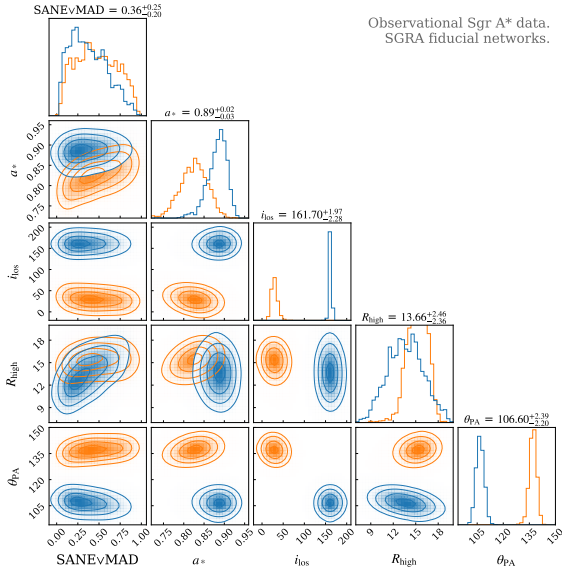
Fig. 5. Same as Figure 4 but for Sgr A* data using our two fiducial Sgr A* BANNs for which the posteriors are shown in blue and orange, respectively. Based on measurements from other instruments (see text), we have a slight preference for the model that predicts $i_{\rm los} > 90°$ (shown in blue), for which we give the numerical parameter ranges in the figure.

Fig. 6. Same as Figure 4 but for Sgr A* data using our dilaton BANN. The models underlying the dilaton training data were only ray-traced for $i_{\rm los} < 90°$ values.

lepton energies could be produced by nonthermal effects such as magnetic reconnection, which would give a different energy distribution function. For the spin, our network infers values in the range of –0.5 to –0.94, clearly preferring retrograde accretion.

Figure 5 shows the results from applying our two fiducial Sgr A* BANNs to the April 7 observational data. The data are inconclusive concerning the magnetic state of the accretion flow. MAD models describe the polarization quantities well, while SANE models are less problematic in terms of excess variability compared to the observations, but see also Salas et al. (2025). A model beyond the standard MAD/SANE dichotomy might work better here. The spin parameter gives a clear preference toward high ~0.8–0.9 values and a prograde accretion flow. Furthermore, the spin axis is oriented close to the line of sight at an angle of about 162° (29° for the other model) and at $\theta_{\rm PA} \sim 106°–$ 137° east of north in the plane of the sky. Due to the symmetry of the GRMHD models, 162° $i_{\rm los}$ corresponds to 18° but for an opposite sense of rotation of the accretion flow. Within the uncertainty from our $i_{\rm los}$ training data sampling in 20° steps, the two BANNs consistently predict small inclination angles of Sgr A*'s spin axis with respect to our line of sight. Evidently, the direction of the accretion flow direction cannot be discerned. The difference between the two position angles inferences can also be understood from the $\theta_{\rm PA} = 90°, 120°, 150°$ sampling of the training data: the inferred values fall on opposite sites of the middle grid value. The low $R_{\rm high} \sim 14$ value corresponds to a dominant emission from the accretion flow via hot electrons in the disk.

These Sgr A* results have been obtained with the level of data calibration described in Event Horizon Telescope Collaboration (2022b) and Janssen et al. (2025a). We note that consistent posteriors with no visible differences are obtained from data that has been processed with additional model-dependent calibration steps described in Section 2.2 of Event Horizon Telescope Collaboration (2022c). We attribute this to the robustness of our BANNs against gain errors in the data, learned from the simulation of data corruption effects in
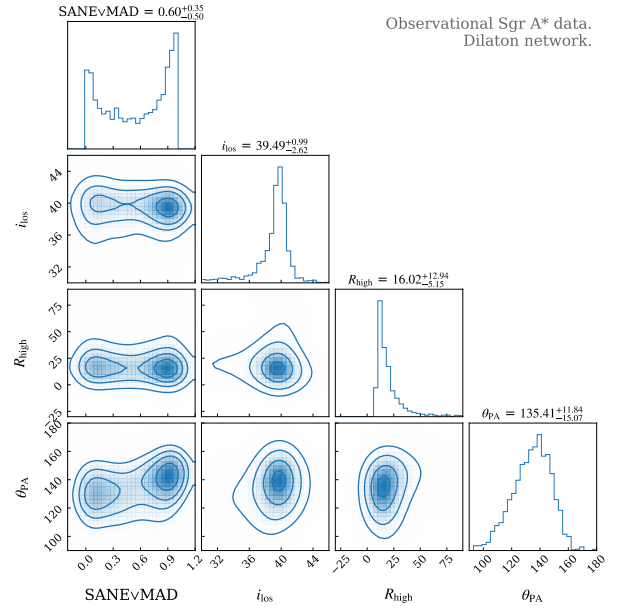
the training data. The Event Horizon Telescope Collaboration (2024) GRMHD scoring results depend on assumptions made about the origin of the Faraday rotation measure (RM). The RM has a constant external component and an internal time-variable component (Goddi et al. 2021; Wielgus et al. 2024). Only the internal component can be simulated in the small computational domain of our GRMHD models. We found that our BANN is not using the constant RM component as a salient model-discriminating data feature; we get identical posteriors when de-rotating the Sgr A* Stokes $Q, \mathcal{U}$ visibilities by 50% or 100% of the overall measured RM = $−4.65 \times 10^5$ rad/m². Applying a time-variable RM to the data on the other hand does change the results. Evidently, our BANN has trained on the internal time-variability of $Q, \mathcal{U}$ phases as discriminating factors for a_* and $i_{\rm los}$. We note that the images across our model library do show differences in their overall electric vector position angle orientations, which is equivalent to having different constant RM components.

Figure 6 is the posterior from the April 7 observational data obtained from our dilaton BANN. All parameters, in particular $R_{\rm high} \sim 16$ and $\theta_{\rm PA} \sim 135°$, agree well with the standard model results. For this model that goes beyond standard GR, also the MAD/SANE classification is inconclusive. We note that the dilaton model considered here is nonrotating and does not reach fully developed MAD states as the amount of magnetic flux accumulating near the event horizon remains modest. The small 10° difference in inclination angle is well within the uncertainties and likely related to the different discrete $i_{\rm los}$ sampling values of the training data. Closest to the inferred values of 29° and 39°, these are $i_{\rm los} = 10°, 30°$ for the standard models and $i_{\rm los} = 20°, 40°$ for the dilaton models, respectively. We note that no $i_{\rm los} > 90°$ mode can be inferred for the dilaton models, as the ray-tracing was only done up to a maximum inclination of 60°.

The consistency of parameter inference between the dilaton and fiducial Sgr A* models is noteworthy, given that the dilaton BANN trained only on Stokes $\mathcal{I}$ data, which we have shown to not work for M87*. We attribute this to the intrinsic dilaton model variability measured across different baselines

over the course of a single very long baseline interferometry (VLBI) observation. With the help of this variability, models with different parameters can be distinguished.

Our individual BANNs are interpolating between training values for many parameters[1], with no wide multimodal posteriors. This latter case is a "failure mode" of our BANNs, when the variational inference runs on data that are difficult to characterize (Janssen et al. 2025b). Compared to GRMHD validation data, wider posteriors are obtained on the observational data. Evidently, the observational data cannot be perfectly described by GRMHD models due to missing physics and/or the incomplete sampling of model parameters. Thus, the observational parameter uncertainties are larger than the BANN validation errors. Yet, GRMHD simulations are currently the best models we have to describe the horizon-scale emission of low-luminosity AGN in a self-consistent manner. Barring the SANE/MAD magnetic state inference, Sgr A* has relatively narrow posteriors even though the training validation errors are larger than for M87*. Without strong jet emission from accelerated particles and with an extremely low accretion rate, the Sgr A* data are quite well described by the ideal GRMHD models.

5. Discussion

The GRMHD models underlying our BANN training data assume the presence of a magnetized turbulent accretion flow surrounding a supermassive compact object. The initial gaseous torus is aligned with the equatorial plane of the black hole (i.e., the accretion disk is not tilted). The gas is assumed to be pure hydrogen. Pair production and radiative cooling processes are not simulated. The electron distribution function is assumed to be thermal, neglecting particle acceleration processes and nonideal MHD processes. Even though our analysis is model-dependent, we sampled a broad parameter space. Thus, it is instructive to put our inference results into perspective.

Our M87* analysis favors MAD models with large R_{high} values and a_* between -0.5 and -0.94, which have powerful outflows and strong synchrotron emission from the jet. The probability density likely peaks at those particular values because they are two neighboring values in our GRMHD training data grid space. We also note that past EHT image scoring analyses have disfavored the MAD $a_* = -0.94$ models (Event Horizon Telescope Collaboration 2019c, 2021b). We thus argue for the "true" spin of a best-fitting GRMHD model to be most likely at an intermediate $-0.94 < a_* < -0.5$ value. The strong preference for a MAD accretion in M87* is in agreement with past EHT analyses. Furthermore, the inferred model parameters satisfy jet power constraints measured at larger spatial scales (Event Horizon Telescope Collaboration 2019c; Nemmen 2019). The black hole counter rotation fits in the picture of M87* being an elliptical galaxy likely affected by past mergers (e.g., Volonteri et al. 2007; Raimundo et al. 2023). Mergers can naturally explain the large spin (e.g., Berti & Volonteri 2008), while the black hole spin-down will not be too extreme in the strongly sub-Eddington accretion of M87*, even for a retrograde MAD flow (e.g., Narayan et al. 2022; Lowell et al. 2024).

Qiu et al. (2023) trained a random forest machine learning model on a few predetermined EHT observables and infer high-spin retrograde models with large R_{high} values for M87*. Our findings are in excellent agreement with Qiu et al., who

have used a similar GRMHD library but without the full forward modeling. In our work, we only considered models where the magnetic field polarity is aligned with the accretion disk angular momentum vector on large scales. Qiu et al. (2023) and Joshi et al. (2024) have shown that these models are preferred over models with anti-aligned polarity. The field polarity mainly affects circular polarization, which does not yield strong model constraints in the 2017 EHT data (Ricarte et al. 2021; Event Horizon Telescope Collaboration 2023).

The high spin value of $a_* \sim 0.8$–0.9 inferred for Sgr A* by our fiducial network agrees with mounting evidence from independent analyses in the literature, which suggest a spin >0.5. From the Eckart et al. (2018) literature overview of several model-dependent radio, near-infrared, and X-ray data analyses, a slight tendency for $a_* > 0.5$ crystallizes. Recent combined Chandra plus VLA modeling results find $a_* = 0.9 \pm 0.06$ when assuming the presence of a collimated outflow (Daly et al. 2024). From the analysis of ALMA light curves, Wielgus et al. (2022b) find hints of a positive spin and Yfantis et al. (2024a) find $a_* > 0.8$, but noted a weak spin-dependence of their results. In early fits of GRMHD models to the Sgr A* spectral energy distribution (SED) and initial VLBI size constraints, high spin values were also preferred (Mościbrodzka et al. 2009). Finally, the best-bet model from our recent EHT analysis has $a_* = 0.94$ (Event Horizon Telescope Collaboration 2024). One should note the fundamental difference of constraint-based EHT modeling compared to our BANN inference. Additionally, the EHT modeling assumed the RM to be external and discarded the model variability problem (Event Horizon Telescope Collaboration 2022d; Wielgus et al. 2022a). We attribute the stark difference in the electron temperature coupling factor – $R_{high} = 160$ of the $a_* = 0.94$ model versus a much lower value inferred here – to these fundamental analysis differences. Similarly, the discrepancy between the prograde accretion flow (positive a_*) inferred here and the preference for a retrograde MAD flow in Joshi et al. (2024) can be traced to the difference of our approach from the standard GRMHD scoring and the different observational data being used. For a detailed discussion of how the black hole spin can be inferred from EHT data, we refer to Ricarte et al. (2023).

We find Sgr A*'s spin axis to be closely aligned with our line of sight, consistent with earlier findings based on GRAVITY polarimetric plus astrometric measurements of flares (GRAVITY Collaboration 2018, 2020, 2023) as well as ALMA light curves (Wielgus et al. 2022b; Levis et al. 2024; Yfantis et al. 2024a). These studied Q–$\mathcal{U}$ loops display a clockwise rotation on the sky. For our two BANNs, the inferred values are $i_{los} = 28.9^{+7.5}_{-6.3}$ degrees and $i_{los} = 161.7^{+2.0}_{-2.3}$ ($18.3^{+2.3}_{-2.0}$) degrees. Taking the Q–$\mathcal{U}$ loop measurements into account, $i_{los} = 162°$ is preferred, as inclinations larger than 90 degrees correspond to a clockwise accretion flow rotation on the sky in our GRMHD models. Yet, it is worth noting that the super- (rather than sub-)Keplerian motion of a hot-spot describing the GRAVITY Q–$\mathcal{U}$ loops (Matsumoto et al. 2020; Yfantis et al. 2024b) speaks for an emitting region outside of the standard GRMHD accretion flow. Matsumoto et al. (2020), Lin et al. (2023), and Antonopoulou & Nathanail (2024) for example successfully fit the polarization loops with outflow models. For prograde accretion, it is expected that hot spots in outflows and/or current sheets outside of the bulk accretion flow would follow the accretion direction of rotation. Thus, our disfavored $i_{los} = 28.9^{+7.5}_{-6.3}$ solution would require wind-fed accretion (e.g., Ressler et al. 2023) scenarios, where the disk angular momentum can change on short timescales. In this case, counterclockwise Q–$\mathcal{U}$ loops would be observed sometimes. In an alternative scenario, flux tubes in a

---

[1] We impose no bound to the parameters our BANNs could infer; in fact it is easy to devise a network that would predict unphysical GRMHD model parameters.

counterclockwise accretion flow may be bent in the opposite direction, leading to entrapped hot spots moving clockwise (Antonopoulou et al. 2025). For the accretion flow model considered in Faggert et al. (2025), see also Özel et al. (2022) and Younsi et al. (2023), $a_* = 0.8$ agrees with the observed Sgr A* image brightness asymmetry for a broad range of sub-Keplerian velocity profiles for $i_{los} = 18°$, while $i_{los} = 29°$ requires a very slow angular rotation. Generally, hot accretion flows are expected to be sub-Keplerian due to pressure gradients.

As we find Sgr A* unlikely to have a MAD accretion disk with a powerful outflow, the direction of a potential large-scale jet would be determined by the interstellar medium and not the black hole spin direction (e.g., Liska et al. 2018; Kwan et al. 2023; Ressler et al. 2023). Yet, Wang & Zhang (2024) show that a past merger with Gaia-Enceladus (Helmi et al. 2018) can reproduce a high a_* in Sgr A* with a low i_{los}, where the BH spin axis is misaligned with the Milky Way's rotation. Generally, a low i_{los} does thus not preclude Sgr A* jet activity to be responsible for the Galactic Fermi/eROSITA bubbles (Sarkar 2024, note in particular the discussion in Section 4). Recently, Ressler et al. (2023) and Galishnikova et al. (2025) have shown that the presence of strong magnetic fields in Sgr A* (Event Horizon Telescope Collaboration 2021a) does not necessarily lead to a MAD state with strong jets.

The inferred $\theta_{PA} \sim 106°–137°$ position angle of Sgr A*'s spin axis matches with the ~135° found by Ball et al. (2021) and $130° \pm 20°$ from Yfantis et al. (2024b) from the modeling of GRAVITY flares. On the other hand, the GRAVITY Collaboration (2023) find ~177° ± 24° from the GRAVITY data, which is however clearly disfavored by Yfantis et al. (2024b). It is not yet understood why the modeling of polarimetric ALMA light curve data yields significantly different PAs in the range of 0° to 57° (Wielgus et al. 2022b; Yfantis et al. 2024a), but note the 180° degeneracy without the astrometry in the ALMA data (Diogo Ribeiro, priv. comm.). Possibly, ALMA measures an emission region from an inflow or outflow farther away, where the PA is not directly related to the black-hole spin axis.[2] As noted by Ball et al., θ_{PA} close to 150° are consistent with the angular momentum axis of a speculative cold disk around Sgr A* (Murchikova et al. 2019). It thus seems more likely that the Doppler-shifted H30α ALMA measurements are indeed signatures of an accretion flow rather than a collimated jet as suggested by Royster et al. (2019) and Yusef-Zadeh et al. (2020). Although, as laid out earlier, a jet in Sgr A* may very well not follow the black hole spin direction on large scales. Relatedly, we note that Sgr A* image asymmetries determined in current 3 mm VLBI studies are not necessarily related to a jet direction. As noted by Issaoun et al. (2019), the intrinsic source structure is highly symmetric when de-scattering methods are applied and the image major axis direction may also follow accretion flow emission. Future mm-VLBI upgrades will likely enable the Sgr A* jet detection through direct imaging (Chavez et al. 2024).

$R_{high} \sim 14$ translates into the presence of relatively hot electrons in the Sgr A* accretion flow, which is in agreement with past SED model-fits (Yuan et al. 2002; Mościbrodzka & Falcke 2013). As noted by Mościbrodzka and Falcke, R_{high} values between 10 and 30 are also predicted by viscous heating processes in shearing box simulations (Sharma et al. 2007). The

MAD models with a magnetic turbulent cascade heating of electrons considered by Mościbrodzka (2025) are most similar to $R_{high} = 10$ images from the standard models in terms of observational characteristics. The fact that no direct detection of a jet from Sgr A* has been made yet, fits into the picture of a source model with low R_{high}, small i_{los}, and no fully developed MAD accretion flow.

6. Conclusions

We produced a comprehensive GRMHD synthetic data library based on the 2017 EHT data, reduced using an improved calibration pipeline. For the first time, we applied a Bayesian artificial neural network trained on our GRMHD library to EHT visibility measurements. Combined with the bootstrapping resampling method, we used our ZINGULARITY networks to perform GRMHD parameter inference with a robust uncertainty estimation.

Through additional validation tests described here and in Janssen et al. (2025b), we found that our networks have a persistent performance: The results are not influenced by noisy data features or the particular choice of (reasonable) network (hyper-)parameters. The strong intrinsic GRMHD model variability is also properly taken into account. By construction, our results are neither affected by assumptions made in the VLBI data reduction strategy, nor the external physical influences of the Sgr A* scattering screen and external RM component. We find our networks to be able to interpolate between the discrete GRMHD parameters from our training data. It will be worthwhile to produce new GRMHD runs with these intermediate parameter values for future in-depth model-data comparisons. Additionally, the predicted accretion rate, jet power, and broadband spectral energy distribution can be studied.

For the M87* data, we infer MAD models with $R_{high} \geq 160$ and a_* between −0.5 and −0.94. For Sgr A*, we infer models that go beyond MAD/SANE with $a_* \sim 0.8–0.9$, $i_{los} \sim 20°–40°$ (corrected for GRMHD symmetry for clockwise rotating accretion flows), $R_{high} \sim 14$, and $\theta_{PA} \sim 106°–137°$. Our results are in broad agreement with the literature, but the inferred position angle of Sgr A*'s spin axis implies 1.3 mm ALMA measurements are picking up significant emission from non-horizon scales. As a next step, we plan to develop interpretable AI methods, building on the reverse engineering tests conducted in this initial study. The goal is to unravel which predictions are driven by which visibility data points.

Finally, we showed how the planned AMT will likely lead to considerable improvements in parameter estimation accuracy for tests of models that go beyond GR. For quantities of direct scientific interest, we can thus predict qualitative improvements from future EHT array upgrades.

Data and code availability

The observational EHT data can be obtained from the `10.25739/kat4-na03` digital object identifier. A single `data_production.sh` script in a dedicated repository[3] can be used to get a fully automated reduction of the observational data, producing the calibrated EHT data used in this work. This calibration is done with the containerized version 7.2.2 of the RPICARD pipeline[4] (tagged as

---

[2] As discussed in Event Horizon Telescope Collaboration (2022d), the question whether ALMA measurements are impacted by a slowly varying extended unresolved structure in Sgr A* is important for the reconciliation of the variability discrepancy between GRMHD models and ALMA light curves.

[3] https://bitbucket.org/M_Janssen/casaeht
[4] https://bitbucket.org/M_Janssen/picard

646d6a189c01b04cfa10077a46650038d61687d9_
25c42c3c75a8334d1be4f72bc56b4344dc1f068e[5]).

The synthetic training data are generated with the SYMBA pipeline[6] (Roelofs et al. 2020). The containerized[7] 49a813d2dc62eac809f3909bee0d38a8b113ffc4 SYMBA version used in this study is based on RPICARD version 7.2.2 and the focalpy38.fd529fd version of the MEQSILHOUETTE[8] software (Blecher et al. 2017; Natarajan et al. 2022).

The availability of the synthetic GRMHD training datasets is described in Janssen et al. (2025a). The availability of the ZINGULARITY code and configuration files needed to instantiate, train, and apply the BANNs is given in Janssen et al. (2025b).

References

Antonopoulou, E., & Nathanail, A. 2024, A&A, 690, A240
Antonopoulou, E., Loules, A., & Nathanail, A. 2025, A&A, 696, A10
Backes, M., Müller, C., Conway, J. E., et al. 2016, in The 4th Annual Conference on High Energy Astrophysics in Southern Africa (HEASA 2016), 29
Ball, D., Özel, F., Christian, P., Chan, C.-K., & Psaltis, D. 2021, ApJ, 917, 8
Berti, E., & Volonteri, M. 2008, ApJ, 684, 822
Blecher, T., Deane, R., Bernardi, G., & Smirnov, O. 2017, MNRAS, 464, 143
Chavez, E., Issaoun, S., Johnson, M. D., et al. 2024, ApJ, 974, 116
Daly, R. A., Donahue, M., O'Dea, C. P., et al. 2024, MNRAS, 527, 428
Doeleman, S., Blackburn, L., Dexter, J., et al. 2019, in Bulletin of the American Astronomical Society, 51, 256
Doeleman, S. S., Barrett, J., Blackburn, L., et al. 2023, Galaxies, 11, 107
Eckart, A., Tursunov, A. A., Zajacek, M., et al. 2018, in Accretion Processes in Cosmic Sources II, 48
Event Horizon Telescope Collaboration (Akiyama, K., et al.) 2019a, ApJ, 875, L1
Event Horizon Telescope Collaboration (Akiyama, K., et al.) 2019b, ApJ, 875, L3
Event Horizon Telescope Collaboration (Akiyama, K., et al.) 2019c, ApJ, 875, L5
Event Horizon Telescope Collaboration (Akiyama, K., et al.) 2019d, ApJ, 875, L6
Event Horizon Telescope Collaboration (Akiyama, K., et al.) 2021a, ApJ, 910, 48
Event Horizon Telescope Collaboration (Akiyama, K., et al.) 2021b, ApJ, 910, L13
Event Horizon Telescope Collaboration (Akiyama, K., et al.) 2022a, ApJ, 930, L12
Event Horizon Telescope Collaboration (Akiyama, K., et al.) 2022b, ApJ, 930, L13
Event Horizon Telescope Collaboration (Akiyama, K., et al.) 2022c, ApJ, 930, L14
Event Horizon Telescope Collaboration (Akiyama, K., et al.) 2022d, ApJ, 930, L16
Event Horizon Telescope Collaboration (Akiyama, K., et al.) 2023, ApJ, 957, L20
Event Horizon Telescope Collaboration (Akiyama, K., et al.) 2024, ApJ, 964, L26
Faggert, J. C., Özel, F., & Psaltis, D. 2025, ApJ, 981, 209
Foreman-Mackey, D. 2016, J. Open Source Softw., 1, 24
Galishnikova, A., Philippov, A., Quataert, E., Chatterjee, K., & Liska, M. 2025, ApJ, 978, 148
García, A., Galtsov, D., & Kechkin, O. 1995, Phys. Rev. Lett., 74, 1276
Goddi, C., Martí-Vidal, I., Messias, H., et al. 2021, ApJ, 910, L14
Gold, R., Broderick, A. E., Younsi, Z., et al. 2020, ApJ, 897, 148
GRAVITY Collaboration (Abuter, R., et al.) 2018, A&A, 618, L10
GRAVITY Collaboration (Bauböck, M., et al.) 2020, A&A, 635, A143
GRAVITY Collaboration (Abuter, R., et al.) 2023, A&A, 677, L10
He, K., Zhang, X., Ren, S., & Sun, J. 2015, arXiv e-prints [arXiv:1512.03385]
Helmi, A., Babusiaux, C., Koppelman, H. H., et al. 2018, Nature, 563, 85
Issaoun, S., Johnson, M. D., Blackburn, L., et al. 2019, ApJ, 871, 30
Janssen, M., Goddi, C., Falcke, H., et al. 2018, in 14th European VLBI Network Symposium & Users Meeting (EVN 2018), 80
Janssen, M., Goddi, C., van Bemmel, I. M., et al. 2019, A&A, 626, A75
Janssen, M., Radcliffe, J. F., & Wagner, J. 2022, Universe, 8, 527
Janssen, M., Chan, C.-k., Davelaar, J., et al. 2025a, A&A, 698, A60
Janssen, M., Chan, C.-k., Davelaar, J., et al. 2025b, A&A, 698, A61
Joshi, A. V., Prather, B. S., Chan, C.-k., Wielgus, M., & Gammie, C. F. 2024, ApJ, 972, 135
Kerr, R. P. 1963, Phys. Rev. Lett., 11, 237
Kwan, T. M., Dai, L., & Tchekhovskoy, A. 2023, ApJ, 946, L42
La Bella, N., Issaoun, S., Roelofs, F., Fromm, C., & Falcke, H. 2023, A&A, 672, A16
Levis, A., Chael, A. A., Bouman, K. L., Wielgus, M., & Srinivasan, P. P. 2024, Nat. Astron., 8, 765
Lin, X., Li, Y.-P., & Yuan, F. 2023, MNRAS, 520, 1271
Liska, M., Hesp, C., Tchekhovskoy, A., et al. 2018, MNRAS, 474, L81
Lowell, B., Jacquemin-Ide, J., Tchekhovskoy, A., & Duncan, A. 2024, ApJ, 960, 82
Matsumoto, T., Chan, C.-H., & Piran, T. 2020, MNRAS, 497, 2385
Mizuno, Y., Younsi, Z., Fromm, C. M., et al. 2018, Nat. Astron., 2, 585
Mościbrodzka, M. 2025, ApJ, 981, 145
Mościbrodzka, M., & Falcke, H. 2013, A&A, 559, L3
Mościbrodzka, M., Gammie, C. F., Dolence, J. C., Shiokawa, H., & Leung, P. K. 2009, ApJ, 706, 497
Mościbrodzka, M., Falcke, H., & Shiokawa, H. 2016, A&A, 586, A38
Murchikova, E. M., Phinney, E. S., Pancoast, A., & Blandford, R. D. 2019, Nature, 570, 83
Narayan, R., Chael, A., Chatterjee, K., Ricarte, A., & Curd, B. 2022, MNRAS, 511, 3795
Natarajan, I., Deane, R., Martí-Vidal, I., et al. 2022, MNRAS, 512, 490
Nemmen, R. 2019, ApJ, 880, L26
Newman, E. T., Couch, E., Chinnapared, K., et al. 1965, J. Math. Phys., 6, 918
Özel, F., Psaltis, D., & Younsi, Z. 2022, ApJ, 941, 88
Prather, B. S., Dexter, J., Moscibrodzka, M., et al. 2023, ApJ, 950, 35
Qiu, R., Ricarte, A., Narayan, R., et al. 2023, MNRAS, 520, 4867
Raimundo, S. I., Malkan, M., & Vestergaard, M. 2023, Nat. Astron., 7, 463
Ramachandran, P., Zoph, B., & Le, Q. V. 2017, arXiv e-prints [arXiv:1710.05941]
Ressler, S. M., White, C. J., & Quataert, E. 2023, MNRAS, 521, 4277
Ricarte, A., Qiu, R., & Narayan, R. 2021, MNRAS, 505, 523
Ricarte, A., Tiede, P., Emami, R., Tamar, A., & Natarajan, P. 2023, Galaxies, 11, 6
Röder, J., Cruz-Osorio, A., Fromm, C. M., et al. 2023, A&A, 671, A143
Roelofs, F., Janssen, M., Natarajan, I., et al. 2020, A&A, 636, A5
Royster, M. J., Yusef-Zadeh, F., Wardle, M., et al. 2019, ApJ, 872, 2
Salas, L. D. S., Liska, M. T. P., Markoff, S. B., et al. 2025, MNRAS, 538, 698
Sarkar, K. C. 2024, A&A Rev., 32, 1
Sharma, P., Quataert, E., Hammett, G. W., & Stone, J. M. 2007, ApJ, 667, 714
Volonteri, M., Sikora, M., & Lasota, J.-P. 2007, ApJ, 667, 704
Wang, Y., & Zhang, B. 2024, Nat. Astron., 8, 1592
Wielgus, M., Marchili, N., Martí-Vidal, I., et al. 2022a, ApJ, 930, L19
Wielgus, M., Moscibrodzka, M., Vos, J., et al. 2022b, A&A, 665, L6
Wielgus, M., Issaoun, S., Martí-Vidal, I., et al. 2024, A&A, 682, A97
Yfantis, A. I., Mościbrodzka, M. A., Wielgus, M., Vos, J. T., & Jimenez-Rosales, A. 2024a, A&A, 685, A142
Yfantis, A. I., Wielgus, M., & Mościbrodzka, M. 2024b, A&A, 691, A327
Younsi, Z., Psaltis, D., & Özel, F. 2023, ApJ, 942, 47
Yuan, F., Markoff, S., & Falcke, H. 2002, A&A, 383, 854
Yusef-Zadeh, F., Royster, M., Wardle, M., et al. 2020, MNRAS, 499, 3909

[5] https://hub.docker.com/r/mjanssen2308/casavlbi_ehtproduction
[6] https://bitbucket.org/M_Janssen/symba
[7] https://hub.docker.com/r/mjanssen2308/symba
[8] https://github.com/rdeane/MeqSilhouette